



OPEN

First principles calculations of the structural, electronic, magnetic, and thermodynamic properties of the Nd_2MgGe_2 and Gd_2MgGe_2 intermetallic compounds

S. Menouer¹, O. Miloud Abid¹, A. Benzair², A. Yakoubi¹, H. Khachai¹ & U. Schwingenschlög³✉

In recent years the intermetallic ternary RE_2MgGe_2 (RE = rare earth) compounds attract interest in a variety of technological areas. We therefore investigate in the present work the structural, electronic, magnetic, and thermodynamic properties of Nd_2MgGe_2 and Gd_2MgGe_2 . Spin-orbit coupling is found to play an essential role in realizing the antiferromagnetic ground state observed in experiments. Both materials show metallicity and application of a Debye-Slater model demonstrates low thermal conductivity and little effects of the RE atom on the thermodynamic behavior.

The examination of intermetallic compounds with Mo_2FeB_2 structure type (space group $P4/mbm$), as ordered variant of the U_3Si_2 structure type, has been the subject of many studies in recent years due to a variety of intriguing physical properties¹. Examples reach from superconductivity to heavy fermion behavior, Kondo lattices, and magnetocalorics². Well-known members of the material class are U_2SnCo_2 and U_2InPt_2 , non-Fermi liquid systems on the verge of long-range magnetic ordering, and the hybridization-gap semiconductor U_2SnRu_2 ³. $\text{Y}_{1.6}\text{Ce}_{0.4}\text{InPd}_2$ and $\text{Lu}_{1.6}\text{Ce}_{0.4}\text{InPd}_2$ show heavy fermion behavior and in Ce_2InRh_2 the Ce atoms realize a mixed valent state with high spin fluctuation temperature⁴. Yb_2AlSi_2 , on the other hand, shows an intermediate valent state⁵. More than 300 intermetallic compounds M_2XT_2 (M = rare earth or actinoid metal; X = Mg, In, Sn, Cd; T = transition metal) are known. The X and T atoms constitute planar $[\text{XT}_2]$ networks such that each X atom is coordinated to four T_2 dumb-bells^{6,7}. The crystal structure can be understood as packing of distorted fragments of AlB_2 and CsCl structure types, which form a network of octahedra and trigonal bipyramids with interstitial sites favorable for H allocation. The M atoms form a planar structure with triangular motif, which, depending on the exchange interaction, can lead to magnetic frustration, as described by the two-dimensional Shastry-Sutherland Hamiltonian $H = J \sum_{NN} S_i S_j + J' \sum_{NNN} S_i S_j$, where S_i represents the magnetic moment at site i ⁸. Magnetic frustration exists when the nearest neighbor interaction J and next nearest neighbor interaction J' are both antiferromagnetic (AF)⁹. Since $J > J'$, nearest neighbor atoms form a network of J -coupled dimers that are coupled by J' . The ground state is a disordered spin liquid with energy gap between the singlet and triplet states or an antiferromagnet with gapless magnetic excitations. Transition is predicted for $J'/J \approx 0.6-0.7$ at 0 K¹⁰, although symmetry arguments suggest that an intermediate state is required, such as a helical magnet or a spin density wave¹¹.

Cermets with Mo_2FeB_2 structure type show excellent wear resistance, low friction to non-ferrous metals, and thermal expansion coefficients close to those of steel. While they are not as strong as the commonly used hard metals¹², the mechanical properties can be improved by Cr and Ni additions. B, V, and Mn additions reduce the grain size and remarkably increase the transverse rupture strength¹³. RE_2MgT_2 (RE = rare earth) compounds are used for lightweight construction in the automobile and aerospace industries¹⁴. They show high corrosion

¹Laboratoire d'Étude des Matériaux et Instrumentations Optiques, Département Matériaux et Développement Durable, Faculté des Sciences Exactes, Université Djillali Liabès de Sidi Bel Abbès, 22000 Sidi Bel Abbès, Algérie. ²Laboratoire de Modélisation et Simulation Multi-échelle, Faculté des Sciences Exactes, Département de Physique, Université Djillali Liabès de Sidi Bel Abbès, 22000 Sidi Bel Abbès, Algérie. ³Physical Science and Engineering Division (PSE), King Abdullah University of Science and Technology (KAUST), Thuwal 23955-6900, Saudi Arabia. ✉email: udo.schwingenschlogl@kaust.edu.sa

resistance and thus have been investigated intensively with respect to their microstructure and mechanical properties¹⁵. The compounds play an essential role as bio-compatible materials for healing or replacing natural bone¹⁶. They are also able to absorb large amounts of H, up to 8 atoms per formula unit, which weakens the magnetism, as the RE–RE exchange interaction and magnetic coupling via the conduction electrons are suppressed (while for U_2MgT_2 the upper limit of H absorption is 2 atoms per formula unit and hydrogenation enhances the magnetism)^{17,18}. Interstitial doping with H atoms, which induces internal pressure and/or modifies the bonding between the other atoms, can be used to tune the crystal and electronic structures, particularly the magnetism, which depends critically on details of the hybridization and charge localization¹⁹.

M_2XT_2 compounds can be magnetocaloric with field-induced magnetic and/or structural transitions, where for $M = RE$ the magnetic structure is determined mainly by the (i) RKKY (Ruderman, Kittel, Kasuya, and Yosida) interaction and (ii) crystalline electric field (which is responsible for magnetic phase transitions, for example, for $RE = Nd$)²⁰. In magnetocaloric ferromagnets/antiferromagnets the entropy change during isothermal magnetization is negative/positive (termed positive/negative magnetocaloric effect). A positive magnetocaloric effect is interesting for magnetic refrigerators and a negative magnetocaloric effect for heat pumps²¹.

In U_2SnT_2 compounds (non-magnetic or magnetic depending on T) the interatomic distance between U and T increases from U_2SnFe_2 to U_2SnCo_2 and U_2SnNi_2 , even though the atomic radius decreases from Fe (1.27 Å) to Co (1.25 Å) and Ni (1.24 Å), and the spin–orbit coupling plays an important role for the electronic states²². While in U_2SnNi_2 the a lattice parameter increases with the temperature and the c lattice parameter decreases, in the cases of U_2SnCo_2 and U_2SnPd_2 both lattice parameters increase²². U_2SnNi_2 shows AF ordering below 25 K with the U moments aligned parallel to the c -axis²³. The band width of the U 5f. states decreases for heavier $T = Co, Ni, Rh, Pd, Ir,$ and Pt ²⁴. Giant magnetoresistance is predicted for U_2SnPd_2 and U_2InPd_2 ²⁵, and specific heat data classify single crystalline U_2SnCo_2 and U_2InPt_2 as non-Fermi-liquid materials²⁶. Enhanced hybridization between the U 5f. and Ni 3d states leads in $U_2Sn(Ni_{1-x}Co_x)_2$ solid solutions for increasing x to a loss of AF ordering at $x = 0.3$ and in $U_2Sn(Ni_{1-x}Pd_x)_2$ solid solutions to a decrease of the Neel temperature (T_N) up to $x = 0.3$, which is reproduced by the RKKY model²². At 1.5 K the U magnetic moments switch from in-plane ordering in U_2SnPd_2 ($2 \mu_B$) to out-of-plane ordering in $U_2Sn_{0.65}Pd_{2.35}$ ($0.9 \mu_B$) due to enhanced hybridization between the U 5f. and Pd 4d states (reduced U–Pd distance)²².

The magnetic behavior of the Ce_2InT_2 compounds is determined by the filling of the T d bands, with Ce being trivalent in Ce_2InCu_2 and Ce_2InAu_2 but not in Ce_2InPd_2 ²⁷. First principles calculations demonstrate that in Ce_2SnPd_2 the hybridization between the Ce 4f. and Pd 4d states is weak (strong localization of the Ce 4f. states and large Ce magnetic moments)²⁶. $Ce_2(In/Sn)Pd_2$ alloys display transitions between AF and ferromagnetic (FM) ground states as a function of the Sn/In ratio^{28,29}. Ce_2PbPt_2 realizes AF ordering below 3.4 K³⁰. Tb_2InCu_2 is FM up to 81 K²⁹, and Nd_2InAu_2 and Tb_2InAu_2 are ferrimagnetic and FM up to 36 and 73 K with magnetic moments of 3.5 and 9.31 μ_B , respectively³⁰. Pr_2InNi_2 and Nd_2InNi_2 undergo second order FM to paramagnetic transitions at 7.5 and 10.5 K, respectively, according to Ref. 31, whereas Ref. 32 reports Nd_2InNi_2 to be AF with $T_N = 8$ K. Nd_2InNi_2 can absorb up to 7 H atoms per formula unit at room temperature, which leads to expansion of the unit cell along the a - and c -axes and compression along the b -axis (orthorhombic structure with space group $Pbam$)³³. The Nd magnetic moment of 3.55 μ_B resembles that of a free Nd^{3+} ion (3.62 μ_B)^{34,35}. Nd_2InNi_2 is an Ising antiferromagnet³⁶.

Tb_2InPd_2 shows a significantly higher $T_N = 32$ K than Pr_2InPd_2 (5 K) and Nd_2InPd_2 (8 K)³⁷, with a spin-reorientation transition at $\mu_0H_c = 4$ T. Ref. 38 confirms $T_N = 29.4$ K for Tb_2InPd_2 . Based on neutron powder diffraction, the Tb magnetic moments of $\mu_{eff} = 10.54 \mu_B$ (aligned along the c -axis) exceed the theoretically predicted value of 9.72 μ_B ^{35,37}. Substitution of In by Pd in Ce_2InPd_2 results in a transition from FM to AF ordering³⁹. The fact that the specific heat of Yb_2InPd_2 is one order of magnitude larger than that of Yb_2InAu_2 is due to a high Yb 4f. density of states at the Fermi level, the intermediate valence of Yb being explained by hybridization with the Pd 4d states⁴⁰. RE_2PbPd_2 compounds with $RE = Ce, Nd, Sm, Gd, Tb, Dy, Ho, Er,$ and Tm show AF ordering at low temperatures (T_N in the range of 3.6–35 K), Pr_2PbPd_2 is a Curie–Weiss paramagnet down to 1.72 K, and Y_2PbPd_2 and La_2PbPd_2 are weak Pauli paramagnets⁴¹. Ce_2PbPd_2 is subject to a weak Kondo effect with a Ce magnetic moment of 2.61 μ_B , and RE magnetic moments of 4.05 and 9.85 μ_B are found for Nd_2PbPd_2 and Tb_2PbPd_2 , respectively⁴¹. Ce_2MgSi_2 shows helical AF ordering at $T_N = 12$ K with magnetocrystalline anisotropy and a Ce magnetic moment of 2.47 μ_B ⁴². An anomaly in the electrical resistivity of Nd_2InGe_2 at 9 K points to AF ordering with a small FM component⁴³.

In the case of the RE_2SnNi_2 compounds the smaller RE elements Ho, Er, Tm, Lu, and Sc result in a Mo_2FeB_2 structure, whereas the larger RE elements Ce, Pr, Nd, Sm, Gd, Tb, Dy, and Y result in an orthorhombic W_2CoB_2 structure (space group $Immm$)^{44,45}. Nd_2SnNi_2 exhibits AF ordering below $T_N = 21$ K (which can be turned into FM ordering by a moderate magnetic field of 0.25 T) and two further magnetic transitions at 17.7 and 14–15 K²⁰. Ce_2SnNi_2 is a Kondo system with $T_N = 4.7$ K and $T_K \approx 8$ K, and Gd_2SnNi_2 and Tb_2SnNi_2 show oscillatory magnetocaloric effects²⁰. Tb_2SnNi_2 transforms under high pressure (8 GPa) and high temperature (1470 K) to the Mo_2FeB_2 structure⁴⁴. In the W_2CoB_2 structure it shows AF ordering below $T_N = 66$ K (Tb magnetic moment of 8.7 μ_B ; very close to a free Tb^{3+} ion) with magnetic transitions at 42 and 8 K (probably coexistence of FM and AF ordering), and a Curie–Weiss behavior above 80 K (Tb magnetic moment of 7.7 μ_B)²⁰. In the temperature range of 5–220 K, Nd_2SnNi_2 and Tb_2SnNi_2 do not reach their theoretical saturation magnetization in a magnetic field of 100 kOe, which may be attributed to a canted magnetic structure²⁰. For the isothermal magnetic entropy change in a magnetic field of 50 kOe values of 7.2, 0.1, 4.6, and 2.8 J/kg K are reported for Nd_2SnNi_2 , Sm_2SnNi_2 , Gd_2SnNi_2 , and Tb_2SnNi_2 , respectively²⁰. Tb_2SnNi_2 shows striking similarities to $(Pr,Ca)MnO_3$, since both these compounds are subject to coexistence of AF and FM ordering at low temperature with a magnetocaloric effect that switches from negative to positive when the temperature increases⁴⁶.

Replacing the transition metal with a main group element has a drastic effect on the RE element and thus on the magnetic properties. To give an example, T_N grows from 49 K in Gd_2MgNi_2 (additional magnetic transitions

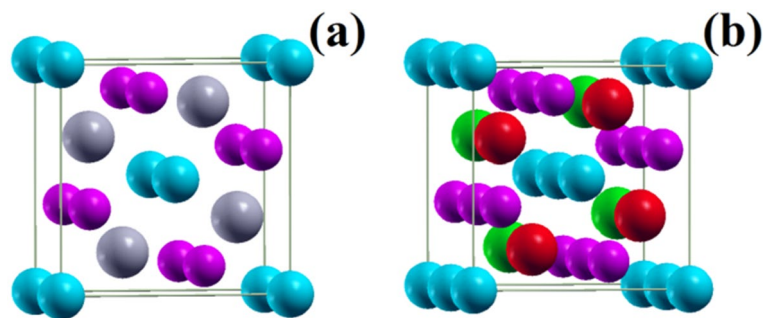


Figure 1. (a) Crystal structure. Gray, blue, and purple spheres represent the RE, Mg, and Ge atoms, respectively. (b) AF ordering of the RE³⁺ ions (green spheres represent spin up and red spheres spin down).

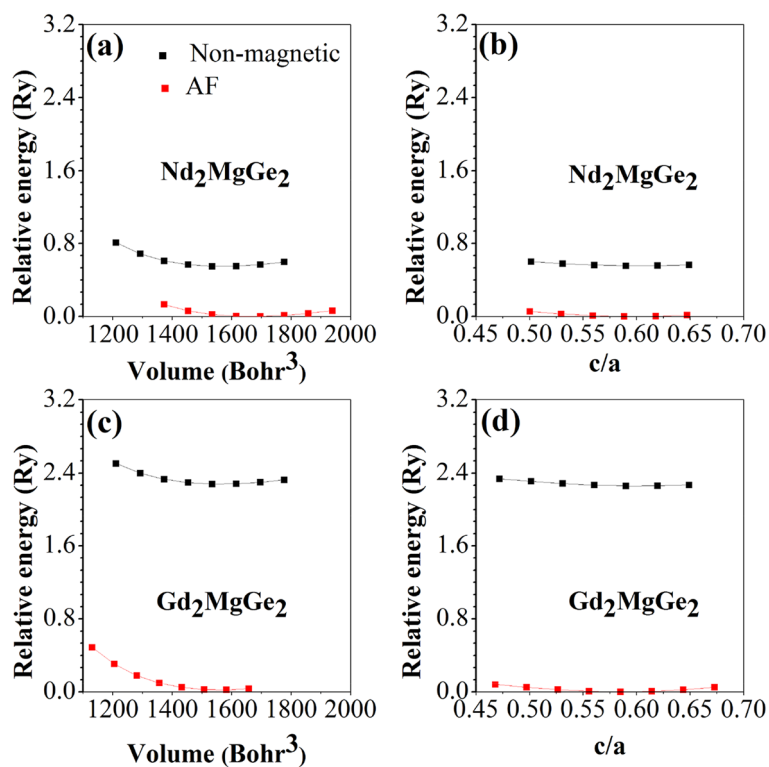


Figure 2. Total energy (a, c) versus volume and (b, d) versus c/a ratio.

at 20.7 and 4.5 K⁴⁷) to 150 K in Gd₂MgGe₂⁴⁸. The RE₂MgGe₂ compounds with RE = Nd, Gd, Tb, Dy, Ho, Er, and Tm show Curie–Weiss paramagnetism at high temperature, while Y₂MgGe₂ and Lu₂MgGe₂ display Pauli-like temperature independent paramagnetism⁴⁹. AF ordering at 14, 13, 32, 55, 24, and 14 K is found for Nd₂MgGe₂, Sm₂MgGe₂, Gd₂MgGe₂, Tb₂MgGe₂, Dy₂MgGe₂, and Ho₂MgGe₂, respectively, while Er₂MgGe₂ and Tm₂MgGe₂ do not undergo magnetic ordering at least down to 5 K⁴⁹. Since the type of magnetic ordering and ordering temperature are determined by the atomic interactions⁵⁰ and there is a lack of detailed understanding, the present work addresses the class of RE₂MgGe₂ compounds from a first principles perspective.

Results and discussion

We use the full potential linear augmented plane wave plus local orbitals software WIEN2k⁵¹, which provides highly accurate results due to the fact that it is an all-electron implementation of density functional theory. The electronic wave functions are expanded in spherical harmonics (up to $l_{\max} = 10$) within non-overlapping muffin-tin spheres centered at the nuclear sites and plane waves (limited by $K_{\max} = 7/R_{\text{MT,min}}$) in the remaining space (interstitial region). The generalized gradient approximation is chosen for the exchange–correlation functional⁵². We employ $6 \times 6 \times 11$ and $6 \times 6 \times 5$ Monkhorst–Pack k -grids in the structural optimizations of unit cells and $1 \times 1 \times 2$ supercells, respectively. The unit cells are non-primitive with two formula units (Fig. 1a). In the supercell calculations spin-polarization is taken into account with the RE atoms coupled ferromagnetically within the ab -plane and antiferromagnetically along the c -axis (Fig. 1b). Densities of states are calculated using

	Nd ₂ MgGe ₂			Gd ₂ MgGe ₂		
	Non-magnetic	AF	Experiment	Non-magnetic	AF	Experiment
<i>a</i>	7.28	7.43	7.41	7.28	7.32	7.29
<i>c</i>	4.37	4.46	4.36	4.36	4.30	4.28
<i>x</i> _{RE}	0.176	0.177	0.178	0.174	0.177	–
<i>x</i> _{Ge}	0.375	0.378	0.379	0.375	0.376	–
<i>V</i> ₀	1565	1661	1616	1561	1559	1536
<i>B</i>	62	53	–	55	70	–
<i>B</i> '	4	5	–	4	4	–

Table 1. Lattice parameters (*a*, *c* in Å), internal parameters (*x*_{RE}, *x*_{Ge}), equilibrium volume (*V*₀ in Bohr³), bulk modulus at 0 K (*B* in GPa), and pressure derivative of the bulk modulus (*B*'). Experimental values from Refs.^{48,49} are given for comparison.

	Nd ₂ MgGe ₂			Gd ₂ MgGe ₂		
	GGA+SOC+OP	Nd ³⁺	Experiment	GGA+SOC+OP	Gd ³⁺	Experiment
2 <i>S</i>	3.1	3	–	6.8	7	–
<i>L</i>	5.6	6	–	0	0	–
<i>J</i>	4	4.5	–	3.4	3.5	–
<i>g</i>	0.7	0.7	–	2	2	–
<i>M</i>	3.1	3.6	3.9	7.7	7.9	8

Table 2. Spin moment (*S*), orbital moment (*L*), total moment (*J*), Landé factor (*g*), and total magnetic moment (*M* in μ_B). Free atom (RE³⁺)⁵⁶ and experimental⁴⁹ values are given for comparison.

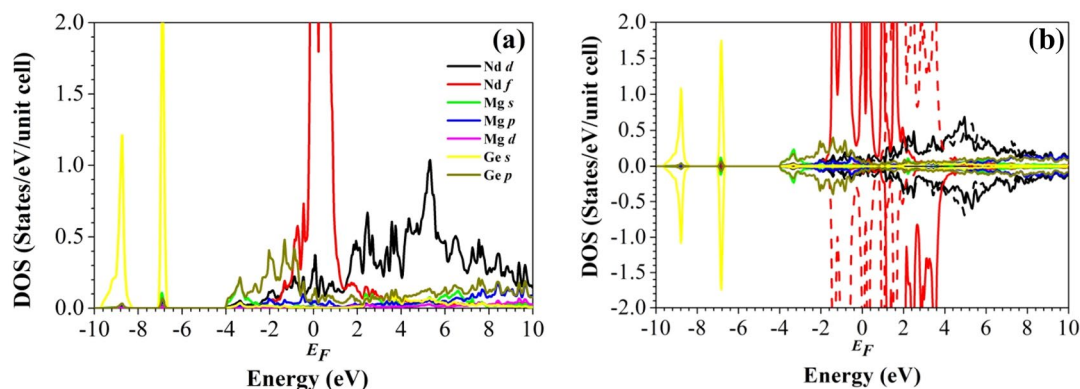


Figure 3. Partial densities of states of Nd₂MgGe₂ in the (a) non-magnetic and (b) AF configurations. Full and dashed lines distinguish between the spin sublattices.

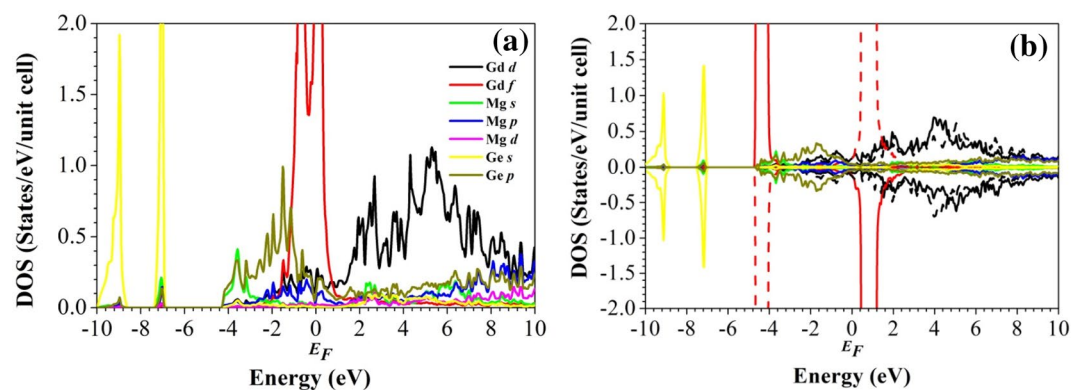


Figure 4. Partial densities of states of Gd₂MgGe₂ in the (a) non-magnetic and (b) AF configurations. Full and dashed lines distinguish between the spin sublattices.

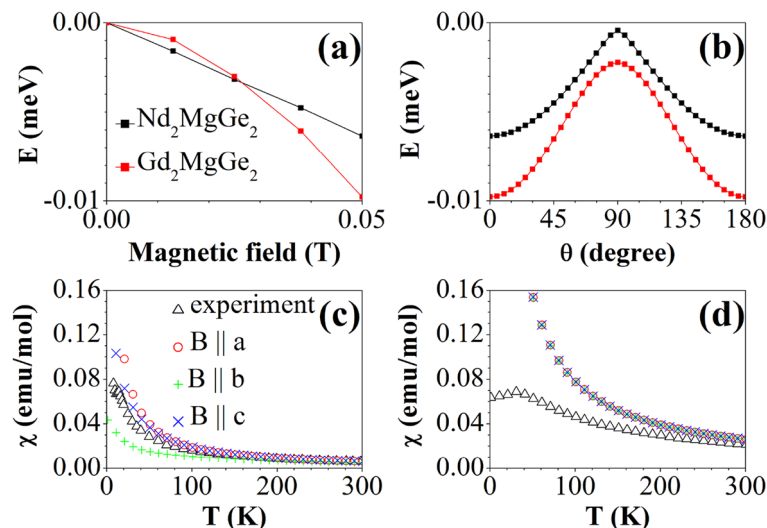


Figure 5. Dependence of the lowest ground state multiplet energy on the (a) strength of an external magnetic field within the *ab*-plane and (b) angle of a 0.05 T magnetic field with respect to the *a*-axis. Temperature dependence of the magnetic susceptibility for (c) Nd₂MgGe₂ and (d) Gd₂MgGe₂.

CP	Nd ₂ MgGe ₂					Gd ₂ MgGe ₂				
	<i>x</i>	<i>y</i>	<i>z</i>	ρ	$\nabla^2\rho$	<i>x</i>	<i>y</i>	<i>z</i>	ρ	$\nabla^2\rho$
Bond1	0	0	0.5	0.013	-0.001	0	0	0.5	0.012	-0.001
Bond2	0.045	0.140	0	0.021	0.038	0.045	0.140	0	0.021	0.038
Bond3	0.486	0.152	0.269	0.029	0.039	0.473	0.144	0.260	0.026	0.040
Bond4	0.282	0.782	0.740	0.033	0.043	0.277	0.777	0.742	0.031	0.031
Bond5	0.5	0	0	0.055	-0.014	0.5	0	0	0.055	-0.014
Ring1	0.044	0.925	0.5	0.012	0.003	0.051	0.920	0.5	0.011	0.003
Ring2	0.256	0.128	0.069	0.014	0.015	0.208	0.107	0.147	0.013	0.017
Ring3	0.5	0	0.5	0.014	0.031	-	-	-	-	-
Ring4	0.405	0.872	0.5	0.015	0.011	0.368	0.899	0.5	0.014	0.011
Ring5	0.431	0.069	0.769	0.024	0.044	0.430	0.070	0.774	0.024	0.037
Cage1	0.448	0.683	0.5	0.011	0.014	0.457	0.666	0.5	0.010	0.009
Cage2	0.174	0.674	0	0.013	0.012	0.175	0.675	0	0.012	0.013
Cage3	0.485	0.985	0.5	0.014	0.030	0.5	0	0.5	0.013	0.029

Table 3. CPs with charge density (ρ in electrons/Bohr³) and its Laplacian ($\nabla^2\rho$ in electrons/Bohr). The names refer to Fig. 6.

a refined $10 \times 10 \times 9$ Monkhorst–Pack *k*-grid and adding spin–orbit coupling by the polarized orbital method to obtain correct magnetic moments^{53,54}.

In the tetragonal unit cell of RE₂MgGe₂ (Fig. 1a) the atoms occupy the Wyckhoff positions RE 4 h ($x_{\text{RE}}, x_{\text{RE}} + 1/2, 1/2$), Ge 4 g ($x_{\text{Ge}}, x_{\text{Ge}} + 1/2, 0$), and Mg 2a (0, 0, 0). Both for non-magnetic and AF configurations, we relax x_{RE} and x_{Ge} at different volumes and fit the total energy to the Murnaghan equation of state⁵⁵ in order to obtain the equilibrium volume (Fig. 2a,b). Then we relax x_{RE} and x_{Ge} at different *c/a* ratios and again fit the total energy to the Murnaghan equation of state in order to obtain the equilibrium *c/a* ratio (Fig. 2c,d) as well as the bulk modulus and its pressure derivative. Table 1 shows that AF ordering significantly modifies the unit cell volume for Nd₂MgGe₂ but not for Gd₂MgGe₂. It turns out that AF ordering results in energy gain of 0.5 eV per unit cell for Nd₂MgGe₂ and 2.3 eV per unit cell for Gd₂MgGe₂ with respect to the non-magnetic solution. We do not further investigate Sm₂MgGe₂, Tb₂MgGe₂, Dy₂MgGe₂, and Ho₂MgGe₂, as no qualitative difference can be expected. Y₂MgGe₂ and Lu₂MgGe₂ are not of interest, because no magnetic ordering is obtained, in agreement with Ref. 49. For Er₂MgGe₂ and Tm₂MgGe₂ our calculations predict magnetic ground states. However, absence of magnetic ordering above 5 K implies that the compounds undergo low temperature phase transitions, i.e., our results are not of experimental relevance and therefore excluded from the following discussions.

The obtained AF lattice constants in Table 1 deviate from the experimental values by less than 0.4% (*a*) and 2.3% (*c*)^{48,49}. They turn out to be smaller for Gd₂MgGe₂ than Nd₂MgGe₂ though Gd is heavier than Nd (lanthanide contraction) and the shortest RE–RE distances within the *ab*-plane (3.72 Å for Nd₂MgGe₂, 3.66 Å for

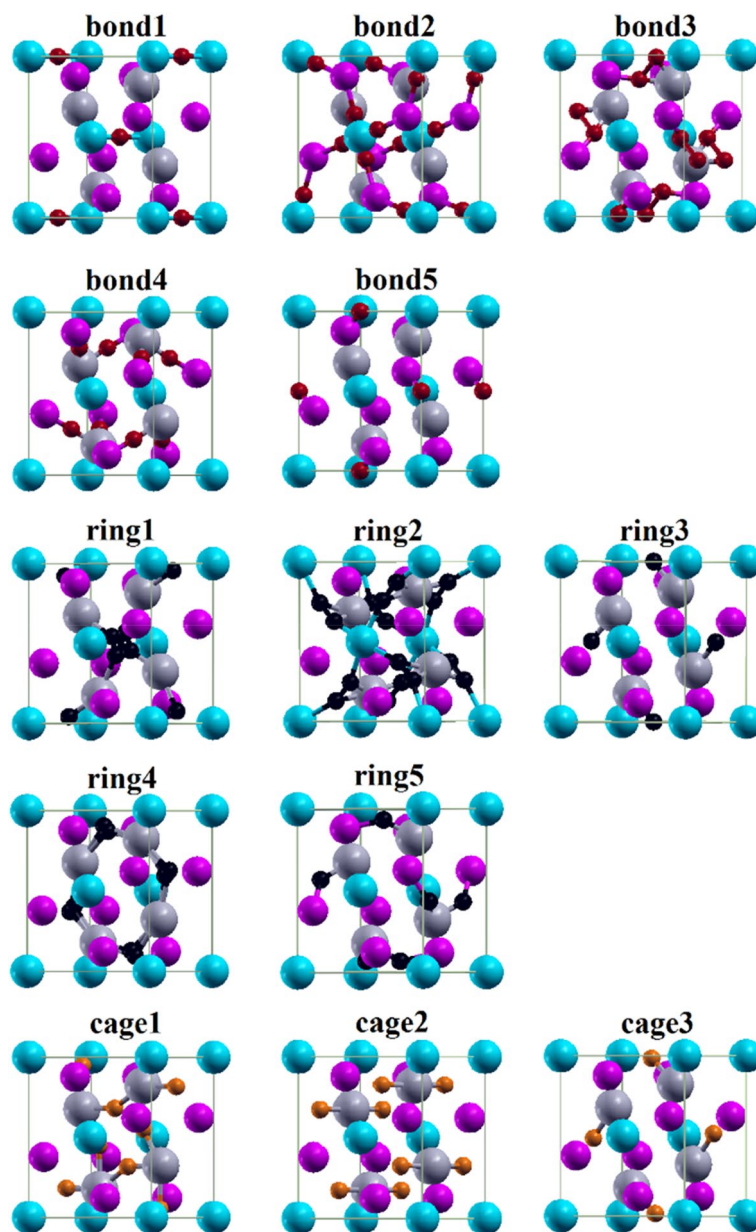


Figure 6. Bond CPs (red spheres), ring CPs (black spheres), and cage CPs (orange spheres). Gray, blue, and purple spheres represent the RE, Mg, and Ge atoms, respectively.

Gd_2MgGe_2) are significantly smaller than those along the c -axis (4.46 Å for Nd_2MgGe_2 , 4.30 Å for Gd_2MgGe_2). This confirms the magnetic structure model of Ref. 49 that the localized RE 4f. spins realize FM ordering within the ab -plane and AF ordering mediated by RKKY interaction along the c -axis. As expected, we find $B \propto V_0^{-1}$, where V_0 is the equilibrium unit cell volume. Rather small values of B reflect softness of the compounds under study. The magnetic moment $M = g\sqrt{J(J+1)}$ depends on the Landé factor $g = 1 + \frac{J(J+1)+S(S+1)-L(L+1)}{2J(J+1)}$ with $J = L \pm S$ for a less/more than half-filled shell⁵⁶. Comparison of the obtained magnetic moments with experiment in Table 2 confirms the validity of our theoretical approach. The fact that they are almost purely of 4f. origin and close to those of free atoms demonstrates localized magnetism.

To study the nature of the chemical bonding, we evaluate the electronic density of states (DOS) in Figs. 3 and 4. We note that the local density approximation yields qualitatively the same behavior (Figure S1 in the Supporting Information) and that the wave function expansions are well converged (Figure S2 in the Supporting Information). For both the non-magnetic and AF configurations of the two compounds we obtain similar results, in particular a finite DOS at the Fermi level, i.e., a metallic state. The high non-magnetic DOS at the Fermi level (mainly Nd/Gd 4f. states) points to magnetism according to the Stoner criterion⁵⁷. The symmetric shape of the AF DOS is due to the absence of a total magnetic moment. The AF DOS shows strong contributions of the Ge 4s states at low energy, the Ge 4p states below the Fermi level, and the Nd/Gd 4f. states above the Fermi level. The Nd 4f. states are found from -2 eV to 4 eV, whereas the Gd 4f. states give rise to pronounced peaks around -4 eV

Atom	Nd ₂ MgGe ₂			Gd ₂ MgGe ₂		
	χ	ΔQ	Ω	χ	ΔQ	Ω
Nd	1.14	0.99	158	–	–	–
Gd	–	–	–	1.20	1.03	147
Mg	1.31	0.93	89	1.31	0.98	89
Ge	2.01	–1.46	189	2.01	–1.53	199
Total	–	–	1564	–	–	1562

Table 4. Pauling electronegativity (χ), oxidation state (ΔQ), and atomic volume (Ω in Bohr³).

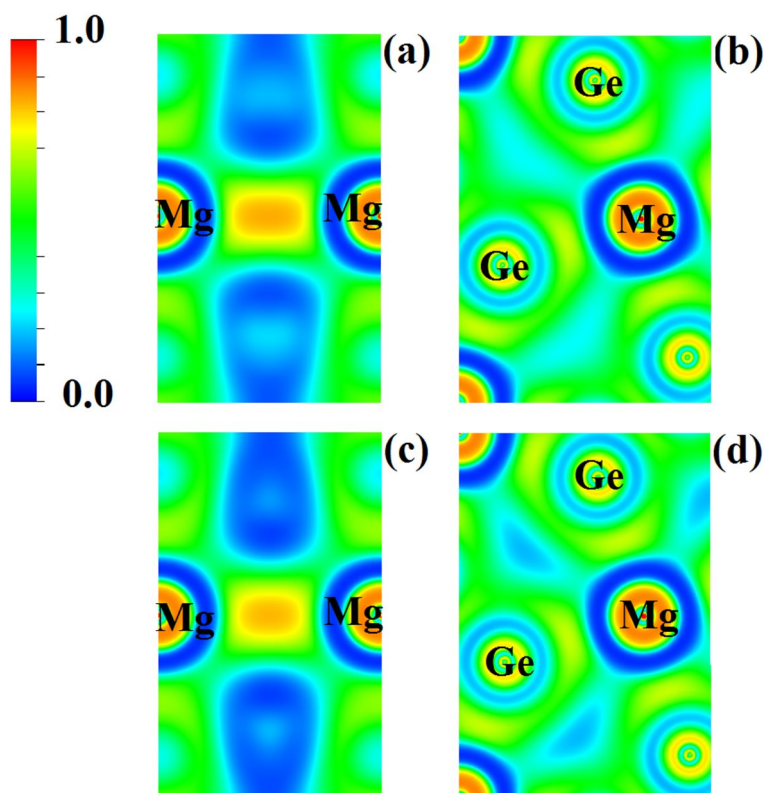


Figure 7. Electron localization function in the (a, c) (200) and (b, d) (001) planes for (a, b) Nd₂MgGe₂ and (c, d) Gd₂MgGe₂.

	α_V	C_V	C_p	B	B_S	V_p	$(\alpha_V)^2 BV_p T$	Θ_D
Nd ₂ MgGe ₂	6	120	124	57	60	796.2	4.1	266
Gd ₂ MgGe ₂	6	121	125	52	53	795.1	4.3	245

Table 5. Properties at 300 K: thermal expansion coefficient (α_V in 10^{–5} K^{–1}), vibrational contributions to the heat capacity at constant volume and pressure (C_V and C_p in J/(mol K)), isothermal and adiabatic bulk moduli (B and B_S in GPa), primitive unit cell volume (V_p in Bohr³), $(\alpha_V)^2 BV_p T$ (in J/(mol K)), and Debye temperature (Θ_D in K).

and just above the Fermi level. As the compounds are isostructural, the nature of the chemical bonding is similar (except for the splitting of the Nd/Gd 4f. states) and the physical properties thus are expected to be comparable.

To better understand the magnetism, we evaluate as dominant perturbation the crystal field splitting of the localized and correlated 4f. states. We follow the methodology of Refs.^{58–62} to extract the crystal field parameters from our first principles calculations and obtain the ground state multiplet energies 0, 2, 13, 15, and 16 meV (first excited state: 245 meV) for the Nd³⁺ ions and 0, 0.01, 0.03, and 0.05 meV (first excited state: 3980 meV) for the Gd³⁺ ions. Nd³⁺ (4f³ electronic configuration) and Gd³⁺ (4f⁷ electronic configuration) are Kramer ions.

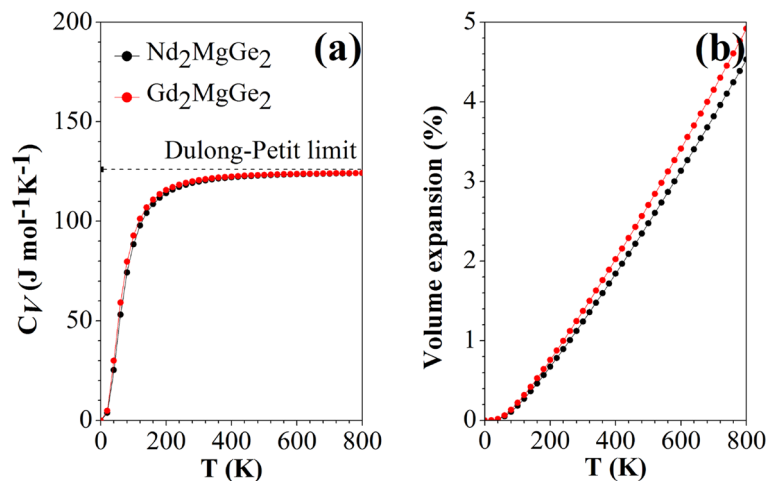


Figure 8. Temperature dependence of the (a) heat capacity and (b) volume expansion (unit cell).

While the ground state of Nd^{3+} ($^4I_{9/2}$, $S=3/2$, $L=6$, $J=9/2$) is split by the crystal field into five Kramer doublets (in agreement with Ref. 63), Gd^{3+} has zero orbital moment in the ground state ($^8S_{7/2}$, $S=7/2$, $L=0$, $J=7/2$) and, consequently, is not influenced by the crystal field in first approximation. The angular dependence of the ground state multiplet energies in a magnetic field aligned within the ab -plane (Fig. 5a,b) shows that a is the easy magnetic axis and b is the hard magnetic axis. The obtained magnetic susceptibilities approach the experimental curve for increasing temperature (Fig. 5c,d).

We analyze the electron density in terms of the quantum theory of atoms in molecules⁶⁴ (CRITIC code⁶⁵) by means of the critical points (CPs), which are categorized into nuclear, bond, ring, and cage CPs according to the Hessian matrix. Table 3 lists the locations and characteristics of all the symmetry-inequivalent CPs. As expected, the CPs are very similar for the two compounds. In Fig. 6 we represent the bond CPs (same order as in Table 3) by red spheres to identify the atoms linked by them. For Nd_2MgGe_2 the Ge–Mg bond CP is closer to Mg (2.03 Å) than Ge (3.41 Å), while the Ge–Nd bond CP is more centered. The electron density at the bond CPs is small and the Laplacian is close to zero (positive in the cases of the Ge–Mg and Ge–Nd bonds, negative in the cases of the Mg–Mg and Ge–Ge bonds; Table 3). For Gd_2MgGe_2 the Ge–Gd bond CP is closer to Gd (2.86 Å) than Ge (3.00 Å). Again the electron density at the CPs is small and the Laplacian is close to zero (positive in the case of the Ge–Gd bonds, negative in the cases of the Ge–Ge and Mg–Mg bonds; Table 3).

Table 4 lists the atomic volumes and corresponding integrated charges. 48% and 51% of the unit cell volume is filled by Ge for Nd_2MgGe_2 and Gd_2MgGe_2 , respectively, 40% and 38% by RE, and 11% by Mg. We find a net transfer of charge from Nd/Gd and Mg to Ge, in agreement with the Pauling electronegativity. The obtained oxidation states deviate significantly from the nominal values of +3 (Nd/Gd), +2 (Mg), and –4 (Ge), confirming a metallic nature⁴⁸, in contrast to the semiconducting charge distribution with neutral Mg proposed in Ref. 66. The global charge transfer is described by the ionicity $c = \frac{1}{N} \sum_{i=1}^N \frac{\Delta Q_i}{OS_i}$ ⁶⁷, where N is the number of atomic sites i and $\Delta Q_i/OS_i$ is the ratio of the actual and nominal oxidation states. The values of 37% and 39% for Nd_2MgGe_2 and Gd_2MgGe_2 , respectively, are indicative of dominant covalent bonding. Indeed, the electron localization function demonstrates strong covalent Mg–Mg bonds (Fig. 7a,c) and the electronic charges in Table 4 in conjunction with Fig. 7b,d point to polarized covalent Mg–Ge bonds. We estimate the degree of metallicity in terms of the electron density flatness $f = \rho_{\min}/\rho_{\max}$, where ρ_{\min} is the minimum electron density (at the cage1 CP) and ρ_{\max} is the maximum electron density (at the bond5 CP)⁶⁵. As $f=1$ represents metallic bonding and $f=0$ represents localized bonding, the obtained values of 20% and 18% for Nd_2MgGe_2 and Gd_2MgGe_2 , respectively, show that metallic bonding plays a limited role.

We use a Debye–Slater model to drive the thermodynamic properties⁶⁸. Table 5 indicates that the two compounds behave similarly although Nd_2MgGe_2 shows slightly larger bulk modulus and Debye temperature. The heat capacity at constant pressure (C_p) turns out to be larger than the heat capacity at constant volume (C_V), consistent with the relation $C_p - C_V = (\alpha_V)^2 B V_p T$, where α_V , B , V_p , and T are the thermal expansion coefficient at constant volume, bulk modulus, volume of the primitive unit cell (Nd_2MgGe_2 : $\frac{1}{2} \times 1592.4 \text{ Bohr}^3$; Gd_2MgGe_2 : $\frac{1}{2} \times 1590.2 \text{ Bohr}^3$), and absolute temperature, respectively. According to Fig. 8a, $C_V \propto T^3$ at low temperature and the Dulong–Petit limit is approached at high temperature. Low Debye temperatures reflect low thermal conductivities and melting temperatures. According to Fig. 8b, the volume expansion starts to become linear in T at about 150 K.

Conclusions

The structural, electronic, magnetic, and thermodynamic properties of the intermetallic compounds Nd_2MgGe_2 and Gd_2MgGe_2 have been investigated by full potential linearized augmented plane wave plus local orbitals calculations, employing the generalized gradient approximation for the exchange–correlation potential. The calculated lattice constants agree well with the available experimental data. Accounting for the spin–orbit coupling turns out

to be mandatory to obtain correct magnetic moments and evaluate the electronic properties. Both compounds are found to combine metallicity with an AF ground state with localized magnetic moments. The chemical bonding turns out to be predominantly covalent. According to a Debye-Slater model, the thermal conductivity is low and the choice of the RE atom hardly affects the thermodynamic behavior.

Received: 8 November 2020; Accepted: 20 April 2021

Published online: 25 May 2021

References

- Villars, P. & Calvert, L. D. (eds.), 2nd edn. <https://searchworks.stanford.edu/view/2016804> (American Society for Metals, 1991).
- Szytula, A. & Leciejewicz, J. *Handbook of Crystal Structures and Magnetic Properties of Rare Earth Intermetallics* (CRC Press, 1994).
- Kaczorowski, D. & Gulay, L. D. Magnetic and electrical properties of a novel compound U_2Pd_2Pb . *J. Alloys Compd.* **419**, 11–14 (2006).
- Mallik, R., Sampathkumaran, E. V., Dumschat, J. & Wortmann, G. Magnetic ordering and spin fluctuation behavior in compounds of the type $Ce_2(Pd, Rh)_2In$. *Solid State Commun.* **102**, 59–64 (1997).
- Gannon, W. J. *et al.* Intermediate valence in single crystalline Yb_2Si_2Al . *Phys. Rev. B* **98**, 075101 (2018).
- Zaremba, V. I., Johrendt, D., Rodewald, U., Nychyporuk, P. & Pöttgen, R. Structure and chemical bonding of Ce_2Ge_2In and Ce_2Pt_2In . *Solid State Sci.* **7**, 998–1002 (2005).
- Wang, B., Liu, Y., Ye, J. & Wang, J. Electronic, magnetic and elastic properties of Mo_2FeB_2 : first-principles calculations. *Comput. Mater. Sci.* **70**, 133–139 (2013).
- Shastry, B. S. & Sutherland, B. Exact ground state of a quantum mechanical antiferromagnet. *Phys. B* **108**, 1069–1070 (1981).
- Miyahara, S. & Ueda, K. Theory of the orthogonal dimer Heisenberg spin model for $SrCu_2(BO_3)_2$. *J. Phys. Condens. Matter* **15**, R327–R366 (2003).
- Havela, L., Mašková, S., Daniš, S., Stelmakhovich, O. & Miliyanchuk, K. Large H absorption in Nd_2Ni_2In ; magnetism in a new structure type. *Mater. Res. Soc. Symp. Proc.* **1216**, W03–W12 (2010).
- Carpentier, D. & Balents, L. Field theory for generalized Shastry–Sutherland models. *Phys. Rev. B* **65**, 024427 (2002).
- Sun, C., Yu, H. & Liu, W. Microstructure, mechanical properties and first-principles calculations of Mo_2FeB_2 -based cermets with Mn addition. *J. Ceram. Soc. Jpn.* **125**, 677–680 (2017).
- Xuming, P., Yong, Z., Shaogang, W. & Qihong, W. Effect of Mn on valence-electron structure and properties of hard phase in Mo_2FeB_2 -based cermets. *Int. J. Refract. Met. Hard Mater.* **27**, 777–780 (2009).
- Aghion, E., Bronfin, B. & Eliezer, D. The role of the magnesium industry in protecting the environment. *J. Mater. Process. Technol.* **117**, 381–385 (2001).
- Kraft, R., Fickenscher, T., Kotzyba, G., Hoffmann, R. & Pottgen, R. Intermetallic rare earth (RE) magnesium compounds $REPdMg$ and RE_2Pd_2Mg . *Intermetallics* **11**, 111–118 (2003).
- Staiger, M., Pietak, A., Huadmai, J. & Dias, G. Magnesium and its alloys as orthopedic biomaterials: a review. *Biomaterials* **27**, 1728–1734 (2006).
- Ourane, B. Recherche Exploratoire de Nouveaux Intermetalliques Ternaires à Base de Magnésium, Application au Stockage d'Hydrogène, Doctoral Thesis, Bordeaux University (2014).
- Miliyanchuk, K., Maskova, S., Havela, L. & Gladyshevskii, R. Influence of hydrogenation on the magnetic properties of Er_2Ni_2Al . *Chem. Met. Alloys* **9**, 169–173 (2016).
- Mašková, S. Structure and Magnetic Properties of f-Electron Compounds and Their Hydrides, Doctoral Thesis, Charles University in Prague, Faculty of Mathematics and Physics (2013).
- Kumar, P., Singh, N. K., Suresh, K. G. & Nigam, A. K. Magnetocaloric and magnetotransport properties of R_2Ni_2Sn compounds (RE = Ce, Nd, Sm, Gd, and Tb). *Phys. Rev. B* **77**, 184411 (2008).
- Proceedings of the First International Conference on Magnetic Refrigeration at Room Temperature, edited by P. W. Egolf, International Institute of Refrigeration, Paris, France (2005).
- Lafargue, D. Structures Magnétiques de Nouveaux Stannures Ternaires à Base d'Uranium ou de Terres Rares T_2M_2Sn (T = RE, U et M = Ni, Pd), Doctoral Thesis, Sciences et Technologies University, Bordeaux I (1997).
- Mašková, S. *et al.* U_2Ni_2Sn and the origin of magnetic anisotropy in uranium compounds. *Phys. Rev. B* **99**, 064415 (2019).
- Prokeg, K., Brfick, E., Nakotte, H., de Chftel, P. F. & de Boer, F. R. Simple calculation of hybridization effects in UTX and U_2T_2X compounds. *Phys. B* **206**(207), 8–10 (1995).
- Richter, M., Zahn, P., Divis, M. & Mertig, I. Giant magnetoresistance in uranium intermetallics: ab initio calculations for U_2Pd_2In and U_2Pd_2Sn . *Phys. Rev. B* **54**, 11985–11988 (1996).
- Lukachuk, M. & Pöttgen, R. Intermetallic compounds with ordered U_3Si_2 or Zr_3Al_2 type structure-crystal chemistry, chemical bonding and physical properties. *Z. Kristallogr.* **218**, 767–787 (2003).
- Hulliger, F. On tetragonal M_2Au_2In and related compounds. *J. Alloys Compd.* **232**, 160–164 (1996).
- Sereni, J. G., Roberts, J., Gastaldo, F. & Giovannini, M. Suppression of the Shastry–Sutherland phase driven by electronic concentration reduction in magnetically frustrated $Ce_{2.15}Pd_{1.95}(Sn_{1-y}In_y)_{0.9}$ alloys. *Phys. Rev. B* **100**, 054421 (2019).
- Sereni, J. G., Roberts, J., G-Bastaldo, F., Gerisso, M. & Giovannini, M. Shastry–Sutherland phase formation in magnetically frustrated $Ce_2Pd_2In_{1-x}Sn_x$ alloys. *Mater. Today Proc.* **14**, 80–83 (2019).
- Kabeya, N. *et al.* Antiferromagnetic ground state and heavy-fermion behavior in Ce_2Pt_2Pb . *Phys. Rev. B* **98**, 035131 (2018).
- Zhang, Z., Wang, P., Ronga, H. & Li, L. Structural and cryogenic magnetic properties of RE_2Ni_2In (RE = Pr, Nd, Dy and Ho) compounds. *Dalton Trans.* **48**, 17792–17799 (2019).
- Maskova, S., Danis, S., Llobet, A., Nakotte, H. & Havela, L. Large magnetocaloric effect in Nd_2Ni_2In . *Acta Phys. Pol. A* **126**, 282–283 (2014).
- Mašková, S. *et al.* Impact of hydrogen absorption on crystal structure and magnetic properties of geometrically frustrated Nd_2Ni_2In . *J. Alloys Compd.* **566**, 22–30 (2016).
- Mašková, S., Havela, L. & Daniš, S. Enormous Hydrogen Absorption in Nd_2Ni_2In , in *WDS'09 Proceedings of Contributed Papers, Part III* 109–112 (2009).
- Mašková, S. *et al.* Magnetic properties of Tb_2Pd_2In . *Single Cryst. Study Solid State Phenom.* **194**, 58–61 (2013).
- Sala, G., Mašková, S. & Stone, M. B. Frustrated ground state in the metallic ising antiferromagnet Nd_2Ni_2In . *Phys. Rev. Mater.* **1**, 054404 (2017).
- Fischer, P. *et al.* Antiferromagnetic rare-earth ordering in the intermetallic compounds R_2Pd_2In (R = Pr, Nd). *J. Phys. Condens. Matter* **12**, 7089–7098 (2000).
- Maskova-Cerna, S. *et al.* New type of magnetic structure in the R_2T_2X group: Tb_2Pd_2In . *J. Phys. Condens. Matter* **32**, 345801 (2020).
- Giovannini, M. *et al.* Effect of nonstoichiometry on the transition from ferromagnetism to antiferromagnetism in the ternary indides $Ce_{1.95}Pd_{2+2x}In_{1-x}$ and $Ce_{2+x}Pd_{1.85}In_{1-x}$. *Phys. Rev. B* **61**, 4044–4053 (2000).

40. Giovannini, M. *et al.* Characterization and physical properties of the indides Yb₂T₂In (T = Cu, Pd, Au). *Intermetallics* **9**, 481–485 (2001).
41. Kaczorowski, D. & Gulay, L. D. Magnetic and electrical properties of RE₂Pd₂Pb (RE = Y, La–Sm, Gd–Tm) compounds. *J. Alloys Compd.* **442**, 169–171 (2007).
42. Dhar, S. K., Manfrinetti, P. & Palenzona, A. Magnetic ordering in CeMg₂Si₂ and Ce₂MgSi₂. *J. Alloys Compd.* **252**, 24–27 (1997).
43. Zaremba, V. I., Kaczorowski, D., Nychporuk, G. P., Rodewald, U. C. & Pöttgen, R. Structure and physical properties of RE₂Ge₂In (RE = La, Ce, Pr, Nd). *Solid State Sci.* **6**, 1301–1306 (2004).
44. Heymann, G. *et al.* High-pressure phases of Tb₂Ni₂Sn and Dy₂Ni₂Sn. *Monatsh. Chem.* **145**, 863–867 (2014).
45. Heying, B., Rodewald, U., Chevalier, B. & Pottgen, R. The stannides RE₂Ni₂Sn (RE = Pr, Ho, Er, Tm)—structural transition from the W₂B₂Co to the Mo₂B₂Fe type as a function of the rare earth size. *Z. Naturforsch. B* **68**, 10–16 (2014).
46. Gomes, A. M., Garcia, F., Guimarães, A. P., Reis, M. S. & Amaral, V. S. Field-tuned magnetocaloric effect in metamagnetic magnetite system. *Appl. Phys. Lett.* **85**, 4974–4976 (2004).
47. Łatka, K., Kmiec, R., Pacyna, A. W., Mishra, R. & Pöttgen, R. Magnetism and hyperfine interactions in Gd₂Ni₂Mg. *Solid State Sci.* **3**, 545–558 (2001).
48. Choe, W., Mille, G. J. & Levin, E. M. Crystal structure and magnetism of Gd₂MgGe₂. *J. Alloys Compd.* **329**, 121–130 (2001).
49. Suen, N., Tobash, P. H. & Bobev, S. Synthesis, structural characterization and magnetic properties of RE₂MgGe₂ (RE = Rare-Earth Metal). *J. Solid State Chem.* **184**, 2941–2947 (2011).
50. Kraft, R. & Pottgen, R. Ternary germanides RE₂Ge₂Mg (RE = Y, La–Nd, Sm, Gd, Tb). *Monatsh. Chem.* **135**, 1327–1334 (2004).
51. Blaha, P., Schwarz, K., Madsen, G. K. H., Kvasnicka, D. & Luitz, J. *WIEN2k: An Augmented Plane Wave+Local Orbitals Program for Calculating Crystal Properties* (Technische Universität Wien, 2001).
52. Perdew, J., Burke, K. & Ernzerhof, M. Generalized gradient approximation made simple. *Phys. Rev. Lett.* **77**, 3865–3868 (1996).
53. Brooks, M. S. S. Calculated ground state properties of light actinide metals and their compounds. *Phys. B* **130**, 6–12 (1985).
54. Eriksson, O., Johansson, B. & Brooks, M. S. S. Meta-magnetism in UCoAl. *J. Phys. C* **1**, 4005–4011 (1989).
55. Murnaghan, F. D. The compressibility of media under extreme pressures. *Proc. Natl. Acad. Sci. USA* **30**, 244–247 (1944).
56. Buschow, K. H. J. & de Boer, F. R. *Physics of Magnetism and Magnetic Materials* (Kluwer Academic Publishers, 2003).
57. Stoner, E. C. Collective electron specific heat and spin paramagnetism in metals. *Proc. R. Soc. A* **154**, 656–678 (1936).
58. Novák, P., Knížek, K. & Kuneš, J. Crystal field parameters with wannier functions: application to rare-earth aluminates. *Phys. Rev. B* **87**, 205139 (2013).
59. Mihoková, E., Novák, P. & Laguta, V. Crystal field and magnetism with Wannier functions: rare-earth doped aluminum garnets. *J. Rare Earth* **33**, 1316–1323 (2015).
60. Novák, P., Kuneš, J. & Knížek, K. Crystal field of rare earth impurities in LaF₃. *Opt. Mater.* **37**, 414–418 (2014).
61. Novák, P., Knížek, K., Maryško, M., Jiráček, Z. & Kuneš, J. Crystal field and magnetism of Pr³⁺ and Nd³⁺ ions in orthorhombic perovskites. *J. Phys. Condens. Matter* **25**, 446001 (2013).
62. Novák, P., Nekvasil, V. & Knížek, K. Crystal field and magnetism with Wannier functions: orthorhombic rare-earth manganites. *J. Magn. Mater.* **358–359**, 228–232 (2014).
63. Popova, M. N. *et al.* Optical spectra, crystal-field parameters, and magnetic susceptibility of multiferroic NdFe₃(BO₃)₄. *Phys. Rev. B* **75**, 224435 (2007).
64. Bader, R. F. W. *Atoms in Molecules* (Oxford University Press, 1990).
65. Otero-de-la-Roza, A., Blanco, M. A., Martín Pendas, A. & Luana, V. Critic: a new program for the topological analysis of solid-state electron densities. *Comput. Phys. Comm.* **180**, 157–166 (2009).
66. Whangbo, M.-H., Lee, C. & Köhler, J. Transition-metal anions in solids and their implications on bonding. *Angew. Chem.* **45**, 7465–7469 (2006).
67. Sanchez, P. M., Pendas, A. M. & Luana, V. A classification of covalent, ionic, and metallic solids based on the electron density. *J. Am. Chem. Soc.* **124**, 14721–14723 (2002).
68. Otero-de-la-Roza, A., Abbasi-Pérez, D. & Luana, V. Gibbs₂: a new version of the quasiharmonic model code. II. Models for solid-state thermodynamics, features and implementation. *Comput. Phys. Commun.* **182**, 2232–2248 (2011).

Acknowledgements

The research reported in this publication was supported by funding from King Abdullah University of Science and Technology (KAUST).

Author contributions

S.M. and O.M.A. conducted the calculations. U.S. contributed to the analysis of the results and writing of the manuscript. All authors reviewed the manuscript.

Competing interests

The authors declare no competing interests.

Additional information

Supplementary information The online version contains supplementary material available at <https://doi.org/10.1038/s41598-021-89042-5>.

Correspondence and requests for materials should be addressed to U.S.

Reprints and permissions information is available at www.nature.com/reprints.

Publisher's note Springer Nature remains neutral with regard to jurisdictional claims in published maps and institutional affiliations.



Open Access This article is licensed under a Creative Commons Attribution 4.0 International License, which permits use, sharing, adaptation, distribution and reproduction in any medium or format, as long as you give appropriate credit to the original author(s) and the source, provide a link to the Creative Commons licence, and indicate if changes were made. The images or other third party material in this article are included in the article's Creative Commons licence, unless indicated otherwise in a credit line to the material. If material is not included in the article's Creative Commons licence and your intended use is not permitted by statutory regulation or exceeds the permitted use, you will need to obtain permission directly from the copyright holder. To view a copy of this licence, visit <http://creativecommons.org/licenses/by/4.0/>.

© The Author(s) 2021